https://doi.org/10.5194/egusphere-2026-5055
Preprint. Discussion started: 25 September 2026

3D surface displacements from digital image correlation on terrain models

Nicolas Oestreicher[1,2,★], Florian Denzinger[1,2,★], and Andrea Manconi[1,2]

[1]WSL Institute for Snow and Avalanche Research SLF, Davos Dorf, Switzerland
[2]Climate Change, Extremes and Natural Hazards in Alpine Regions Centre CERC, Davos Dorf, Switzerland
★These authors contributed equally to this work.

Correspondence: Nicolas Oestreicher (nicolas.oestreicher@slf.ch)

Abstract. We present a methodology to retrieve 3D surface displacement based on Digital Image Correlation (DIC) applied to multitemporal terrain models. Our approach has been developed to overcome the DIC limitation in the vertical component of the displacement field when horizontal shifts are larger than the grid sampling. To validate the performance, we applied the approach to two terrain models acquired over the Brienz/Brinzauls landslide, where surface displacements affect the entire slope with heterogeneous amplitudes and directions. The comparison with in-situ measurements shows that DIC can accurately retrieve horizontal and vertical displacements, providing a clear representation of the spatial extent of the mass movement, as well as an accurate distinction of the internal landslide compartments. Our results are in good agreement with those obtained using a state-of-the-art point correlation method, but require less preprocessing and computational effort. Thus, the proposed DIC strategy can be considered as a valid alternative for measuring 3D surface displacements in scenarios where multitemporal terrain models are available.

1 Introduction

Landslides pose significant hazards to human life and infrastructure worldwide (Froude and Petley, 2018). However, in many cases, catastrophic slope collapses are preceded by a period of slope deformation and creep (Agliardi et al., 2020). It is therefore critical to develop efficient tools to track and monitor pre-failure slope deformation to predict the potential volume of landslide compartments that might fail catastrophically (Loew et al., 2017). In addition, the temporal evolution of the landslide displacement rate can inform about its reactivity to triggering factors and its readiness to fail catastrophically (Petley et al., 2005). Among the available remote sensing methods, Digital Image Correlation (DIC) has been widely applied for measuring surface displacements from imagery. DIC is a technique that measures changes in the position of intensity patterns between digital images acquired over the same scene at different times (Peters and Ranson, 1982; Sutton et al., 1983). The technique was originally developed in experimental mechanics to measure material deformation under laboratory conditions (Chu et al., 1985; Sutton et al., 2009). The principle consists of subdividing a reference image into small overlapping windows and finding their best-matching position in a second image. The positional shift between acquisitions yields the displacement field in the image reference system. Two main algorithmic implementations are commonly applied in DIC. In the spatial domain, Normalised Cross Correlation (NCC) evaluates a similarity score between a reference patch and a displaced candidate region,

https://doi.org/10.5194/egusphere-2026-5055
Preprint. Discussion started: 25 September 2026

with normalisation providing robustness to illumination and contrast variations (Lewis, 2001). In the frequency domain, the cross-power spectrum of two images is computed via Fast Fourier Transform (FFT) and the displacement is encoded in the peak of the resulting correlation surface, at substantially lower computational cost (Kuglin and Hines, 1975; Leprince et al., 2007; Heid and Kääb, 2012).

DIC methods have been applied in the past decades to measure surface displacements associated with different geophysical processes at local scales, e.g., earthquakes, volcanic activity, and slope instability. Such studies include processing of optical satellite imagery at a regional scale (Debella-Gilo and Kääb, 2011; Heid and Kääb, 2012; Stumpf et al., 2014; Kääb et al., 2017), radar satellite imagery (Casu et al., 2011; Manconi et al., 2014, 2024), aerial images (Casson et al., 2003), orthophotographs obtained from manned (Delacourt et al., 2004) or unmanned aerial vehicles (Lucieer et al., 2014), and images from time-lapse cameras (Travelletti et al., 2012). In general, the goal is to retrieve two-dimensional displacement fields; however, some studies were designed to capture the full three-dimensional displacement by combining DIC or offset-tracking with methods such as Digital Elevation Model (DEM) differencing or laser scanning point cloud correlation (Travelletti et al., 2014; Zhou et al., 2015; Delorme et al., 2020; Bickel and Manconi, 2022; Fu et al., 2025; Hanagan et al., 2026).

DIC can also be applied to the hillshade representation of DEMs (Fey et al., 2015) to retrieve horizontal displacements across the full extent of the terrain model, with spatial detail limited by the product sampling distance and the DIC correlation window size. Retrieving the three-dimensional displacement vector requires an additional step. A DEM is defined on a fixed Eulerian grid (Eringen, 1967; Pastor et al., 2008); thus, DEM differencing measures changes at fixed horizontal positions. This can be representative of the vertical displacement only if the horizontal shift between the multitemporal DEMs is smaller than the ground sampling distance (GSD). When significant horizontal motion occurs, DEM differencing introduces systematic errors in the evaluation of vertical displacements. A correction for this bias is established in the tectonic geodesy literature, where horizontal fault slip across sloping terrain is known to introduce an artifact into the measured vertical offset of a fault scarp (Mackenzie and Elliott, 2017). This correction has been applied to coseismic DEM differencing by shifting the post-event elevation model according to an independently measured horizontal displacement field, before differencing (Zhou et al., 2015; Delorme et al., 2020; Hanagan et al., 2026). This correction step has also been applied to landslide monitoring cases using a grid-based feature tracking tool (Fey et al., 2015), but it has not become standard practice in current DEM-based DIC workflows. Despite, alternative approaches to retrieve 3D displacements have been used, by correlating point-clouds (PCC) directly in three-dimensional space (Aryal et al., 2012; Lague et al., 2013; Nissen et al., 2014; James et al., 2017; Anders et al., 2019; Gojcic et al., 2020; Winiwarter et al., 2021; Chanut et al., 2026; Wang et al., 2026) with recent extensions to deep learning-based feature tracking (Gojcic et al., 2021; Kenner et al., 2022; Wang et al., 2026). Working in a Lagrangian framework (Eringen, 1967; Pastor et al., 2008), these methods avoid the horizontal geometric bias; however, they require dense, high-quality acquisitions and distinctive three-dimensional geometric features. On the other hand, DIC on DEMs operates on a widely available, regularly gridded product and is thus computationally efficient.

In this work, we propose a DEM-based DIC workflow that explicitly corrects for the bias introduced by the large horizontal motion in the vertical component through a shift-back procedure. After explaining the rationale of the method, we apply the approach at the Brienz/Brinzauls landslide, Switzerland (Figure 1), and validate the results using ground monitoring data. This

https://doi.org/10.5194/egusphere-2026-5055
Preprint. Discussion started: 25 September 2026

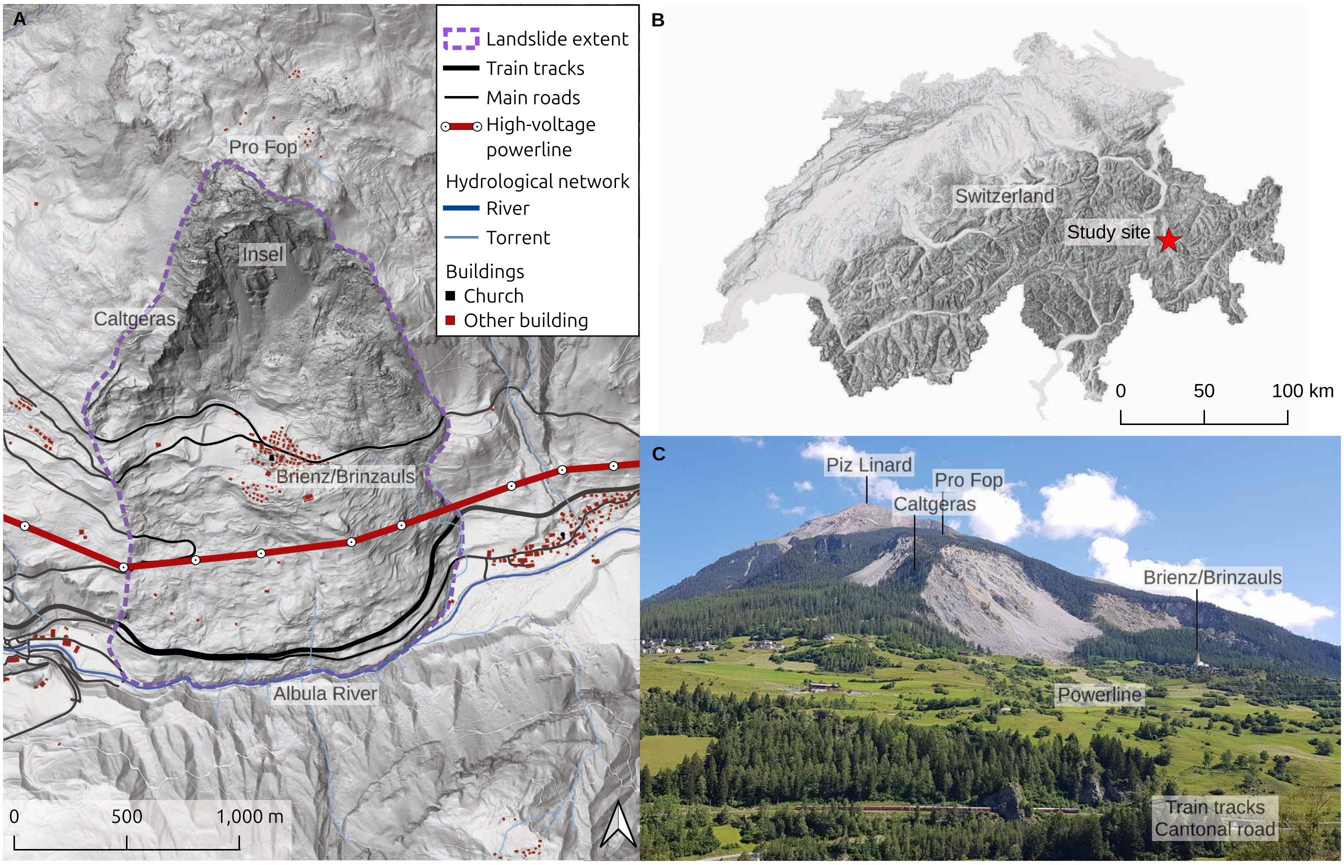

Figure 1. A: Map view of the Brienz/Brinzauls landslide, including location tags used in this study, hydrologic network, and human infrastructures crossing the landslide. These include a high-voltage power line, train tracks, a cantonal road, and buildings. **B:** Overview of the study area in Switzerland (red star). **C:** Picture of the landslide from the South, with elements found on the map in A for the situation. Picture taken in June 2020 by Nicolas Oestreicher. The background map and buildings in **A** and **B** are taken from the Federal Office of Topography Swisstopo (2024).

60 location has been selected as a test site due to the large spatial variability in surface displacement magnitude and direction and the excellent coverage with ground monitoring points, i.e., GNSS and reflectors measured via total station. There, we also compare the performance between our method and a well-established point cloud correlation method, showing the advantages and potential limitations of both approaches.

https://doi.org/10.5194/egusphere-2026-5055
Preprint. Discussion started: 25 September 2026

2 Study Area

2.1 The Brienz/Brinzauls landslide, Graubünden, Switzerland

The Brienz/Brinzauls landslide is a large deep-seated landslide affecting the homonymous village in eastern Switzerland, canton Graubünden (Figure 1). The landslide has been active for thousands of years (Loew et al., 2025), and one of its compartments, called Igl Rutsch, was creeping rapidly before coming to rest in the second half of the 19th century (Heim, 1932). The landslide is crossed by a major high-voltage power line, a cantonal road, and a train line (Figure 1). Together with the village's presence on moving ground, these at-risk elements and the increased velocity triggered a large-scale monitoring program implemented in the early 21st century (Manconi et al., 2024). Among other methods, rockfall events were tracked using Doppler radar (Schneider et al., 2023), a ground-based radar, several GNSS stations, total station reflectors, and time-lapse cameras were installed (Loew et al., 2025). In addition, several boreholes and geophysical methods helped estimate the depth and characteristics of the landslide (Figi et al., 2022; Häusler et al., 2022; Borgeat et al., 2025).

Two distinct parts of the landslide complex have been identified, one below the village ("Rutschung Dorf") moving at a rate up to 1–$2\,m/yr$, and one uphill ("Rutschung Berg"), moving significantly faster, i.e., several meters per year. In particular, one compartment called "Insel" (Loew et al., 2025) collapsed in June 2023, and the debris covered the road leading from Vazerol to Brienz, NW of the village, stopping at only a few tens of meters from the buildings (Loew et al., 2025). After the failure event, the surface velocities in the Rutschung Berg had several phases of decelerations and accelerations, with a renewed critical phase in November 2025 which led to a minor slope failure. At the time of writing, velocities have decreased substantially compared to the period before the 2023 event. Maximum velocities are in the order of $2.5\,m/yr$, thus one order of magnitude slower. Moreover, in the Rutschung Dorf area, velocities have sharply decreased, with maximum values being now below $0.1\,m/yr$, due to the impact of dewatering obtained via a drainage gallery currently under finalization (https://www.albula-alvra.ch/infobrienzerrutsch).

The period preceding the June 2023 collapse is particularly interesting, because the Brienz landslide exhibited large gradients in surface deformation, both in amplitude and direction. Between 2020 and 2022, the displacement range is in the order of $0.1\,m$ in the lowest part of the landslide to values exceeding $20\,m$ in the Insel compartment, thus more than 3 orders of magnitude within the same slope. Displacement direction is mainly southwards; however, some compartments exhibit SE or SW directions locally, with a spreading pattern near the toe of the landslide at the bottom of the valley (Manconi et al., 2024).

2.2 UAV surveys and photogrammetry

We consider data acquired with Uncrewed Aerial Vehicles (UAV) to estimate landslide displacement over a period of 2 years. The first UAV flight took place on 21 February 2020 between 11:00 and 14:30 local time with an eBee X and a S.O.D.A. $20\,MP$ camera with a $28\,mm$ lens. A total of 1362 pictures were taken. The shutter speed was usually at $1/1000\,s$ but sometimes decreased to $1/320\,s$, the aperture ranged from f/2.8 to f/6.3 (rarely $> f/3.5$), and ISO ranged from 125 to 800 (rarely above 200). The second flight was performed on 16 March 2022 with a WingtraOne GenI and a Sony RX1RM2 $42\,MP$ camera with a $35\,mm$ lens. 2049 pictures were taken. The shutter speed was fixed at $1/2000\,s$, the aperture was fixed at f/5.6, and

https://doi.org/10.5194/egusphere-2026-5055
Preprint. Discussion started: 25 September 2026

ISO ranged from 100 to 1000 (rarely above 400). Both flights were processed in Agisoft Metashape with version 2.3.1 build 22416. Image alignment was done considering the settings: Accuracy "High", Key Point limit of 40'000 and a Tie points limit of 4'000, using 4 (2020) and 5 (2022) ground control markers for georeferencing. Depth maps were computed with Quality set to "High" and the Filtering mode set to "Mild". The DEM and point cloud were exported at a resolution of $0.1\,m$. The exported DEMs were interpolated to fill any remaining no-data gaps, giving spatially continuous rasters suitable for frequency-domain image correlation.

2.3 GNSS and TPS data

The surface displacement at the Brienz/Brinzauls landslide has been monitored since 2009 by ground-based systems, most of them being GNSS and total station reflectors. Among all GNSS and total station reflectors installed at Brienz/Brinzauls, we selected locations that were measured around the times of the drone flight acquisitions used in this study. We considered measurements on the days of the drone flights, as well as in the 10 days preceding the flights. We retained 26 reflectors, all measured on the days of the drone flights, and 12 GNSS stations (Figure B1). Among the GNSS stations, 3 were not continuously recording their position, but were measured 10 days prior to the first drone flight in February 2020 and one day prior to the drone flight in 2022. These three stations (12, 13, and 12160230, see Figure B1) are located in the lower part of the landslide, below the village; hence, the shift caused by the 10-day difference is considered negligible relative to the displacement measured over the two years of the temporal window considered. The 12 GNSS stations used in this study are situated in or below the Brienz/Brinzauls village (6 stations) or close to the backscarp of the landslide at Plateau and Caltgeras (6 stations). Total station reflectors are distributed across the slope, with some points situated in slow-moving or stable parts of the landslide, while others are near or on the fast-moving Insel compartment. The reflector 206 measured a 3D displacement of $21.1\,m$ between February 2020 and February 2022. Reflector 708, just south of 206, measured $15.5\,m$, and these two are the fastest-moving points recorded in this time frame. Conversely, the four reflectors in the East of the Insel compartment, above the old Igl Rutsch compartment, were displaced by less than $0.1\,m$ during the two years of this study and are the most stable ground control points (Figure B1 for stations' location).

3 Methods

3.1 Three-dimensional surface displacement retrieval from multi-temporal DEMs

The method applied in this work estimates the full three-dimensional surface displacement field from two DEMs, which are resampled onto a common regular grid, retaining only their spatial overlap. First, we perform DEM preprocessing and convert to an image representation, i.e., a multidirectional hillshade computed by averaging eight shaded-relief images calculated at $45°$ azimuth intervals with a constant solar elevation angle of $45°$. Averaging over all azimuths suppresses directional illumination artifacts and produces a contrast-balanced representation of the surface morphology regardless of terrain aspect. A 3×3 median filter is applied to suppress residual high-frequency noise. Working directly with raw elevation values is disadvantageous for

https://doi.org/10.5194/egusphere-2026-5055
Preprint. Discussion started: 25 September 2026

image correlation because gradual topographic changes produce low-contrast, spatially coherent patterns that degrade the ability to localize matching features. We therefore transform each multidirectional hillshade into an image representation that emphasizes local surface texture, i.e., into an orientation image by retaining only the local gradient direction of the hillshade (Dematteis and Giordan, 2021). This gradient representation yields sharp, stable edges that persist across the two acquisitions and is particularly robust against the high-frequency noise and small-scale illumination inconsistencies that are inherent in high-resolution UAV-derived topographic data. We note that using orthomosaics in DIC leads to artefacts associated with shadows, changes in colors, etc. Surface models are significantly less impacted by these problems and, therefore, more suitable for DIC applications. The same preprocessing step is applied identically to both DEMs before any matching is performed. In the following, we present the details of the DFT-based DIC processing used for initial alignment (co-registration) and horizontal displacement estimation, and subsequently the vertical component retrieval by shifting back the secondary DEM. All analyses were performed in the Swiss National Coordinate Reference System (EPSG:2056, Swiss LV95), consistent with the input DEMs.

3.1.1 Digital Image Correlation (DIC), DFT-based horizontal displacement estimation

Horizontal shifts between multitemporal DEMs (associated to east-west and north-south displacements) are estimated by using a sliding window Discrete Fourier Transform (DFT) image-matching procedure (Guizar-Sicairos et al., 2008). A small rectangular patch is extracted from the orientation image of the primary DEM, and the corresponding region of the secondary orientation image is searched for the best-matching position using the cross-power spectrum. The shift between each patch pair is determined from the peak of their cross-correlation, with subpixel precision achieved by upsampling the cross-power spectrum around its peak (Kuglin and Hines, 1975; Guizar-Sicairos et al., 2008). The correlation window is stepped across the image with a fixed step size, producing a spatially dense displacement field. The row and column offsets are then converted to metric east-west and north-south displacements by multiplying by the target grid spacing. When two drone flights cover the same area, they may not perfectly overlap in stable regions: small errors in GNSS positioning, sensor-specific biases, or residual inaccuracies in the photogrammetric bundle adjustment can introduce a bulk planimetric offset between the two datasets. If left uncorrected, this offset would appear as a displacement signal throughout the final product. An optional co-registration step can therefore be applied to estimate and remove residual misalignment prior to image correlation (Bickel et al., 2018). The shift is estimated by computing the cross-power spectrum of the two orientation images over a stable reference region and locating its peak, applying the same DFT-based matching principle. Because no ground displacement is expected in the reference region, offsets detected there are considered of instrumental origin. At Brienz/Brinzauls, ground displacement affects nearly the entire area covered by the UAV surveys, so the stable reference window had to be placed outside the landslide boundary on a geomorphologically stable terrain to the west (in a patch of approximately 200×200 m). Offset in this patch was estimated at half-pixel precision. The global coregistration step serves to correct rigid shifts introduced by GNSS uncertainties and/or photogrammetric processing artefacts. Local distortions are not corrected and are not expected to play a major role.

Because the Brienz/Brinzauls landslide exhibits surface displacements spanning several orders of magnitude across the slope, the input GSD and the DIC window size can impact the accuracy of the results. Larger windows integrate more surface

https://doi.org/10.5194/egusphere-2026-5055
Preprint. Discussion started: 25 September 2026

texture, tolerate larger displacements, and are less sensitive to noise, but smooth out spatial gradients in the displacement field. Smaller windows preserve spatial detail but require stronger local texture to produce a reliable correlation peak. To evaluate the sensitivity of the retrieved displacement field to these two key parameters, we conducted a systematic parametric analysis. Three GSDs were considered: $0.1\,m$ (the native resolution at which the DEMs were produced), $1\,m$, and $10\,m$. For each resolution, eight DIC processing steps considering different correlation window sizes were tested: 8×8, 16×16, 32×32, 64×64, 128×128, 256×256, 512×512, 1024×1024. The results of this systematic evaluation are reported in Appendix A.

The stride between the moving windows was set to 75 % overlap between adjacent windows. A 50 % overlap would satisfy the Nyquist criterion for spatial sampling of the displacement field; however, the higher 75 % overlap deliberately oversamples the output grid, increasing the density of retrieved displacement vectors and improving the visual continuity of the displacement results. A DFT upsampling factor of 10 was applied throughout, upsampling the cross-power spectrum around its peak and yielding a theoretical displacement precision of 1/10$^{\text{th}}$ pixel (0.01 m at 0.01 m GSD and 1 m at 10 m GSD).

3.1.2 Vertical component retrieval

DEM of Differences (DoD) subtracts elevation values at fixed grid locations between the two acquisitions, assuming that the same patch of ground is captured at each location at both epochs. On a moving slope, this assumption is not valid. The surface has translated horizontally, so the pixel at a given location in the secondary DEM no longer corresponds to the same ground feature as in the primary DEM. This fixed-grid, Eulerian approach introduces an apparent elevation change on sloping terrain even when no real vertical motion has occurred. The steeper the terrain and the larger the horizontal displacement, the more this bias dominates the elevation difference. Figure 2 illustrates this effect with a synthetic Gaussian hill displaced by a known 3D offset (panels A–B): The Eulerian DoD yields a pronounced dipole artefact centred on the hill crest (panel C); the amplitude is driven entirely by local slope and horizontal displacement, not by true vertical change of the hill. The spatial extent of this artefact and its correction are shown as two-dimensional maps in Appendix Figure C1. To address this problem, we apply a procedure referred to as "shift back". Each patch of the secondary DEM is rigidly translated back by the DIC-estimated horizontal displacement, realigning the features with their estimated location in the primary DEM. Because the displacement is applied as a rigid shift per correlation window, the correction is most effective where the displacement field is approximately constant within each window. As shown in panel C in Figure 2, this correction recovers the expected vertical displacement signal. Subtracting the realigned secondary DEM from the primary DEM then yields the vertical displacement component. Since the shift-back is applied as a rigid translation per correlation window, neighbouring windows can be shifted by slightly different amounts, introducing block-wise discontinuities at patch boundaries in the resulting vertical displacement field. Thus, a 9×9 median filter is applied to mitigate this artefact. The shift back procedure allows to remove the effect of horizontal surface shift and to retrieve the local scale vertical displacement, while preserving spatial heterogeneities over the slope. The shift-back approach is an alternative to a point-wise reconstruction of the vertical displacement by finding the height of displaced points onto the secondary DEM through interpolation. The latter approach still produces potential inaccuracies, as demonstrated by our synthetic test in Appendix C; thus, the shift-back procedure provides more accurate retrieval of the vertical displacements.

https://doi.org/10.5194/egusphere-2026-5055
Preprint. Discussion started: 25 September 2026

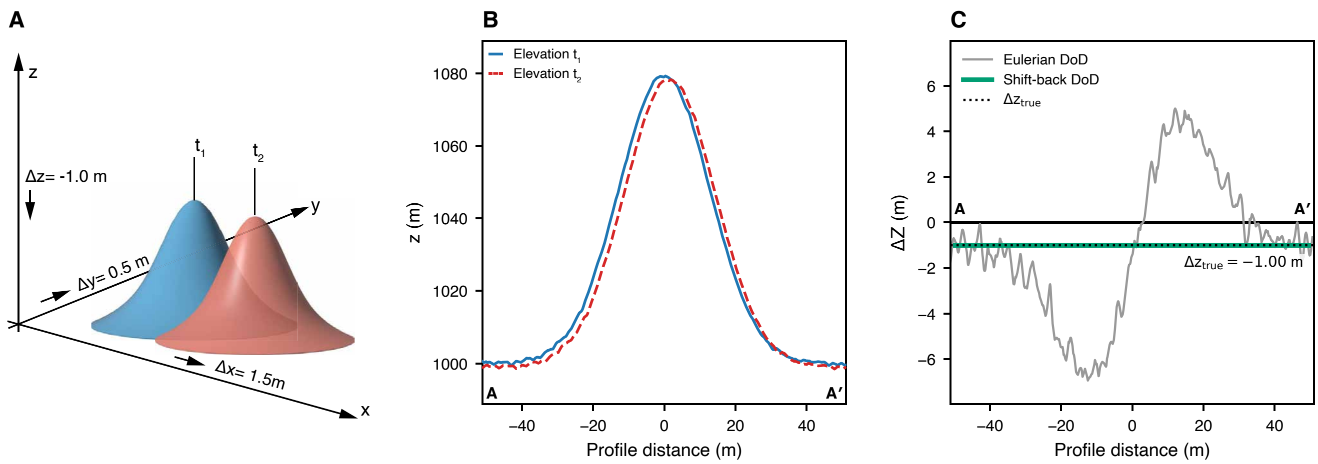

Figure 2. Synthetic validation of the shift-back procedure for vertical displacement retrieval. Two Gaussian-shaped DEMs were generated with a known applied 3D displacement ($\Delta x = 1.5\,\mathrm{m}$, $\Delta y = 0.5\,\mathrm{m}$, $\Delta z = -1.0\,\mathrm{m}$) and a spatially correlated surface texture superimposed on both DEMs to provide realistic DIC matching features. **A:** Overview of the synthetic DEM pair; the horizontal displacement shifts the hill crest from t_1 (blue) to t_2 (red). **B:** Elevation profiles at t_1 and t_2 extracted along the cross-section A-A′ through the hill apex, illustrating the offset of the terrain surface between the two epochs. **C:** Eulerian and shift-back DoD along A-A′ profile: the standard fixed-grid elevation difference (Eulerian DoD) yields a pronounced dipole artefact centred on the hill crest, whose amplitude and sign are controlled by local slope and horizontal displacement magnitude rather than by true vertical change; rigidly translating the t_2 surface back by the DIC-estimated horizontal displacement before differencing (shift-back DoD) removes the dipole artefact and recovers the true vertical displacement (dotted line, $\Delta z_{\mathrm{true}} = -1.0\,\mathrm{m}$).

3.1.3 3D displacement and post-processing

The east-west, north-south, and vertical displacement components are finally combined at each correlation window centre to retrieve a full three-dimensional displacement vector. The vectors are defined on a regularly spaced grid at the window step interval and are interpolated onto the native GSD. To remove outliers, we apply a neighbourhood-similarity outlier filter, similar to the other existing filtering approaches (Kääb et al., 2005; Scherler et al., 2008; Stumpf et al., 2014; Bickel et al., 2018). For each point, the N nearest neighbours within a maximum search distance are identified. Points with fewer than N neighbours within this distance are discarded. The displacement magnitude and azimuth of each remaining point are then compared to the arithmetic mean magnitude and circular mean azimuth of its neighbours, and the point is rejected if its magnitude deviates from the neighbourhood mean by more than a magnitude threshold, or if its azimuth deviates from the neighbourhood mean direction by more than an angular threshold. Points are evaluated in descending order of displacement magnitude, so that the largest vectors are tested first, with increased likelihood of having sufficient neighbours to pass the filter. For the DIC results shown hereafter, this filter was applied, requiring 9 neighbours within a radius of 4.24 times the distance between two points (3

https://doi.org/10.5194/egusphere-2026-5055
Preprint. Discussion started: 25 September 2026

times the diagonal distance between points), with a magnitude difference between the point and the median of its neighbours of 5 m and a direction difference threshold of 90°.

3.1.4 Comparison between DIC and Point-Cloud Correlation (PCC) processing

In order to understand the potential and the limitations of our DIC approach, we considered a state-of-the-art Point-Cloud Correlation (PCC) approach already applied to retrieve 3D displacements at landslides. Feature-to-Feature Supervoxel-based Spatial Smoothing (F2S3) (Gojcic et al., 2020) is a deep-learning-based method for estimating three-dimensional surface displacement vector fields directly between point clouds, without requiring an intermediate gridded representation such as a DEM. It uses interest operators to detect the most suitable points in a given area. We use it here as an independent, point-cloud-based benchmark against which to compare our DIC approach. Details about the F2S3 software, its use, and recommended parameters can be found in Gojcic et al. (2020). Several preprocessing steps were needed in our case due to the large size of the point clouds (~ 624 and ~ 534 million points for the 2020 and 2022 clouds, respectively). F2S3 has difficulty coping with such large datasets, so it was necessary to run the analysis on data subsets. We cut the point clouds into 3 subsets with a buffer distance at boundaries to avoid any boundary effects ($25\,m$ buffer in our case). F2S3 requires the point cloud coordinates format to be short, so we translated the point clouds to the origin. Then, each region was run with a voxel size of $1\,m$ and no maximum displacement magnitude. Afterwards, we cut the $25\,m$ buffer zones from the boundaries of all the resulting point clouds, merged them, and translated the results back to the original coordinate system. Finally, given the high density of the F2S3 point cloud, we applied the same neighbourhood-similarity outlier filter described in Section 3.1.3, requiring ≥ 50 neighbours within a $\leq 50\,m$ search radius, with a magnitude threshold of $1\,m$ and a direction threshold of $15°$, evaluated in descending order of 3D displacement magnitude. As a result, we obtained 3D displacement measurements on $1'291'078$ points.

4 Results

The DIC sensitivity analysis performed (see section A) confirms observations by Hermle et al. (2023). The resolution and window size must be adjusted so that the largest displacement in the study area, where the surface retains some coherence, is contained within a single correlation window. However, our results also show that using the native DEM resolution of 0.1 m increases the noise level, therefore producing larger errors for known points. In the specific example of Brienz/Brinzauls, we found that a GSD of 1 m per pixel and a window size of 64×64 pixels are the optimal settings to achieve the best agreement with the in-situ data. Expert judgement is necessary to select the best DIC parameters, but correlating high-resolution DEMs (e.g., 0.1 m) when the displacement magnitudes are large (e.g., over 10 m) might not always be beneficial. Thus, all the DIC results presented and discussed hereafter are based on the input DEMs with a GSD of 1 m and a window size of 64×64 pixels. Further justifications for this choice are reported in the appendix A.

https://doi.org/10.5194/egusphere-2026-5055
Preprint. Discussion started: 25 September 2026

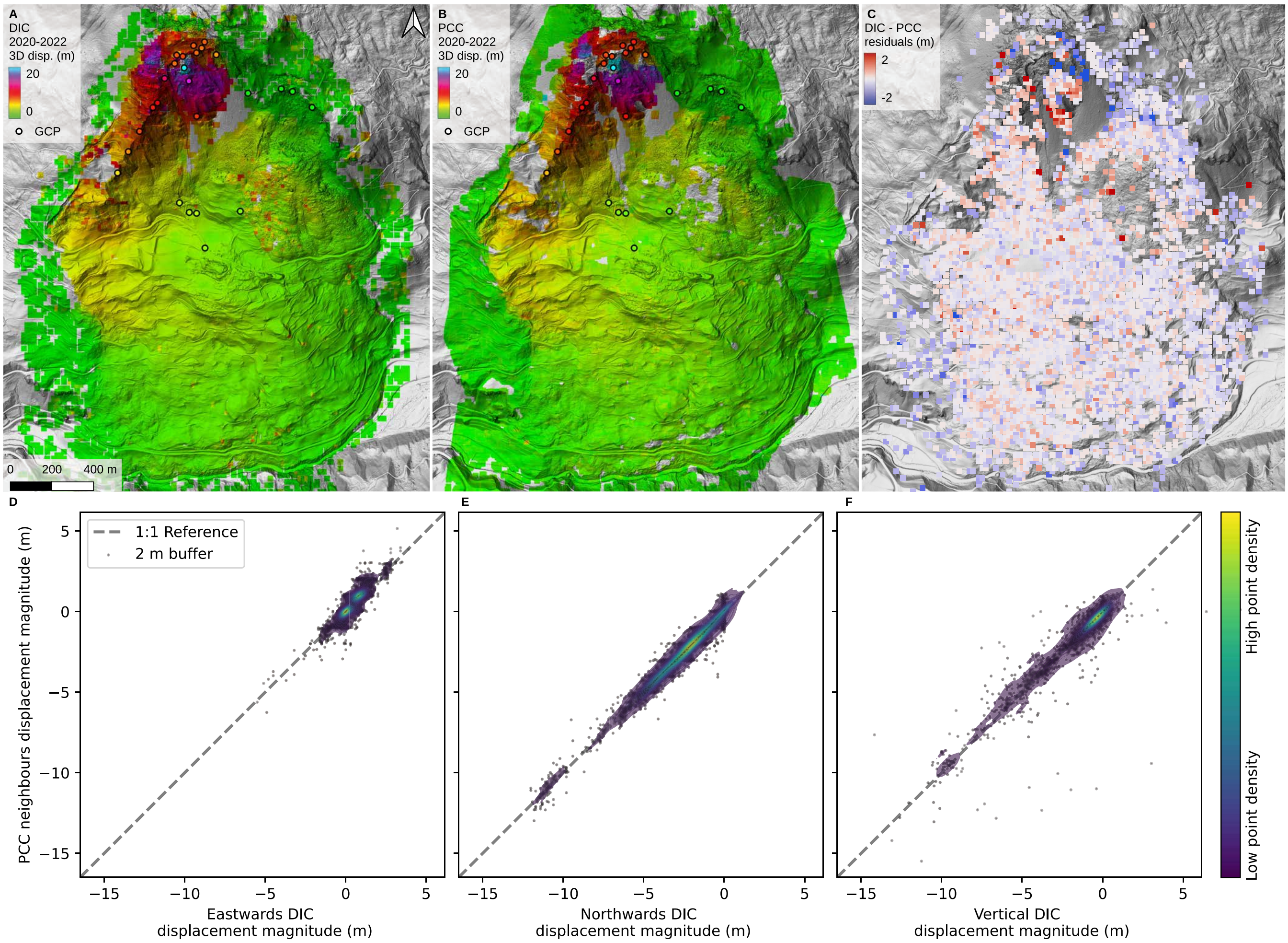

Figure 3. A: DIC 3D displacement magnitude compared to ground-based station displacement (coloured dots). **B:** Same for PCC 3D displacement magnitude. **C:** Residuals between DIC and PCC 3D displacement magnitudes. **D:** Scatter plot comparing displacements measured with DIC and PCC, with 1:1 line for reference Eastwards; **E:** Northwards; **F:** upwards. The background map in **A**, **B**, and **C** is taken from the Federal Office of Topography Swisstopo (2024).

https://doi.org/10.5194/egusphere-2026-5055
Preprint. Discussion started: 25 September 2026

4.1 2020-2022 displacement of the Brienz/Brinzauls landslide

Figure 3 shows the results obtained applying our DIC procedure (panel 3A) and compares them with the PCC processing (panel 3B). The spatial extent of the landslide and the main features impacting the "Rutschung Berg" and "Rutschung Dorf" are clearly mapped by both methods. We note that the coverage of the DIC method is slightly more extensive, particularly in vegetated areas. Both methods produce a comparable extent of the landslide compartments that are moving at different velocities. Both can capture the full range of velocities, except for some compartments in the centre of the landslide, where decorrelation due to complete changes of the surface between the two drone flights prevented measurements with any method presented in this study. The residuals in Figure 3C show that PCC tends to overestimate the displacement in stable areas (e.g., around the landslide). At such locations, we performed manual measurements of displacement between the two model acquisitions and found that they generally agree better with the displacement obtained using DIC. PCC is thus generally more sensitive to vegetation changes, which induced some noise in the data. The residuals between the two methods are further analysed in Figure A1 in the Appendix, which shows that the median values are close to 0 in all directions. The three panels in Figure 3D-F exhibit a decomposition of the displacement in the three spatial directions, comparing values obtained from DIC against nearby PCC features. In both the horizontal and vertical directions, most of the data lie near the 1:1 reference line, except for a few outliers.

Some differences in the compartments can be identified by differences in displacement magnitude or direction relative to their surroundings. At the top of the landslide, South of Pro Fop, there is a plateau that moved $8.5\,m \pm 1.2\,m$ (median and interquartile range of DIC, $8.8\,m \pm 1.1\,m$ for PCC) between 2020 and 2022. The azimuth direction of the displacement field in this compartment is $184 \pm 11^\circ$ (clockwise from North, $179 \pm 15^\circ$ for PCC), and the median dip direction of this part of the slope is about $-51 \pm 11^\circ$ from horizontal ($-52 \pm 6^\circ$ for PCC). Below this plateau, there is a compartment that is the fastest-moving part of the slope (cyan colours in Figure 3A). At this location, near reflector 206, displacements are measured at $18.8\,m \pm 3.1\,m$ ($20.9\,m \pm 2.2\,m$ for PCC) to the S ($177 \pm 11^\circ$ for DIC, $176 \pm 14^\circ$ for PCC), and with a dip of $-48 \pm 6^\circ$ ($-54 \pm 3^\circ$ for PCC). Further downslope, the displacement magnitude and dip angles diminish but remain elevated around $14.9\,m \pm 1.3\,m$ ($14.9 \pm 0.9\,m$ for PCC) to the SSE (azimuth $167 \pm 2^\circ$, $167 \pm 4^\circ$ for PCC, dip of $-40 \pm 4^\circ$, $-40 \pm 2^\circ$ for PCC), until reaching a part of the slope where DIC results are inaccurate due to decorrelation (i.e., large differences in surface properties between the two epochs), likely due to the presence of moving debris below the bedrock cliffs. Directly below, the displacement magnitudes and dip drop respectively to $2.8\,m \pm 0.6\,m$ (PCC: $2.7 \pm 0.9\,m$) and $-21 \pm 11^\circ$ (PCC: $-20 \pm 8^\circ$). Around the Brienz/Brinzauls village, displacements over the two years of this study were measured at $2.7\,m \pm 0.5\,m$ (PCC: $2.9 \pm 0.8\,m$) with a dip angle of $-9 \pm 5^\circ$ (PCC: $-9 \pm 6^\circ$) and a direction to the SSE (DIC: $164 \pm 4^\circ$, PCC: $162 \pm 13^\circ$). However, on the west side of the village, a zone was moving with a median dip angle of $2 \pm 4^\circ$ (PCC: $1 \pm 3^\circ$), locally moving slightly upward, in contrast to the other slope compartments. At Caltgeras, a decorrelated patch is visible, but this is associated with the poorer quality of the 2020 surface model in this zone, which prevents accurate detection of changes. Finally, the lower part of the landslide, near the road and train tracks, shows a spreading pattern. The western part of the landslide was displaced by $1.7\,m \pm 1.0\,m$ (PCC: $1.8 \pm 1.0\,m$) towards S (DIC: $183 \pm 10^\circ$, PCC: $181 \pm 6^\circ$) with a dip angle of $-13 \pm 11^\circ$ (PCC: $-13 \pm 8^\circ$), while the eastern

https://doi.org/10.5194/egusphere-2026-5055
Preprint. Discussion started: 25 September 2026

part was displaced by $1.3\,m \pm 0.5\,m$ (PCC: $1.4 \pm 0.7\,m$) towards ESE (DIC: $127 \pm 15\,°$, PCC: $134 \pm 20\,°$) with a dip angle of $-12 \pm 11\,°$ (PCC: $-13 \pm 11\,°$) between 2020 and 2022.

4.2 Validation with independent measurement methods

We compare the displacement results obtained from DIC and PCC to the displacements measured in-situ, near ground control points (GNSS and reflectors measured with the total station). Figure 4A to C shows map views comparing displacements at the specific locations in magnitude and direction. Horizontal displacements are displayed as arrows, while colours depict vertical displacements. In general, both methods agree well with ground control points and with each other. However, little deviations are noted, for example at the four reflectors in the NE sector, situated close to the backscarp of the active landslide. There, the total station measures little ($0.047 \pm 0.003\,m$) displacement towards the mountain, whereas DIC ($0.14 \pm 0.09\,m$), and PCC ($0.172 \pm 0.126\,m$) overestimate displacement with directions towards the valley.

The scatter plots in panels D-F in Figure 4 show that our DIC approach agrees well with ground measurements (1:1 line) in areas affected by centimetric displacements, as well as in local points affected by displacement in the order of tens of meters. At some locations, we observe larger uncertainties in the vertical component. For instance, the reflectors 403 and 702 have standard deviations exceeding $5\,\mathrm{m}$ in the vertical direction. At both locations, there are 3 samples from DIC within $16\,\mathrm{m}$ of the reflectors to calculate the standard deviation, including one sample situated at the nearby cliff, with a much larger negative displacement due to partial cliff collapse. The larger uncertainty for these reflectors likely reflects spatial variations of vertical displacement around reflectors situated near vertical cliffs.

The panels G, H, and I show that PCC also agrees well with ground measurements, both for small and large displacements. The results of PCC are points corresponding to features that appear in both point clouds. Therefore, there are ground control points where too few features were found in their vicinity. We progressively increased the search radius for PCC features that could be attributed and observed that ground control points with no features within a surrounding $10\,\mathrm{m}$ resulted in significant deviations from the ground measurements. The two stations with larger deviations from the 1:1 line and a buffer radius of $10\,\mathrm{m}$ are the GNSS sites 6005 and 6006. Finally, the pink dot with a buffer radius of $50\,\mathrm{m}$ (hence no features detected near the ground control point) is reflector 602, situated at the edge of the plateau, South of Pro Fop. The majority of the features retained in this $50\,\mathrm{m}$ circle are situated in a compartment of the landslide that was moving significantly more than the plateau above. It is therefore likely that the discrepancy reflects the local differences observed at this location.

5 Discussion

The results obtained from the analysis of the time period 2020-2022 at the Brienz/Brinzauls landslide demonstrate the capacity of DIC to measure 3D slope displacements accurately. The method could recover displacement from centimeters up to $20\,\mathrm{m}$ over the same slope. The ability to accurately identify gradients across several orders of magnitude is important for describing the spatial patterns of displacement and landslide compartments. DIC can be used to track landslide compartments experiencing a potential evolution towards catastrophic collapse, and that, together with expert knowledge, can help assess the potential

https://doi.org/10.5194/egusphere-2026-5055
Preprint. Discussion started: 25 September 2026

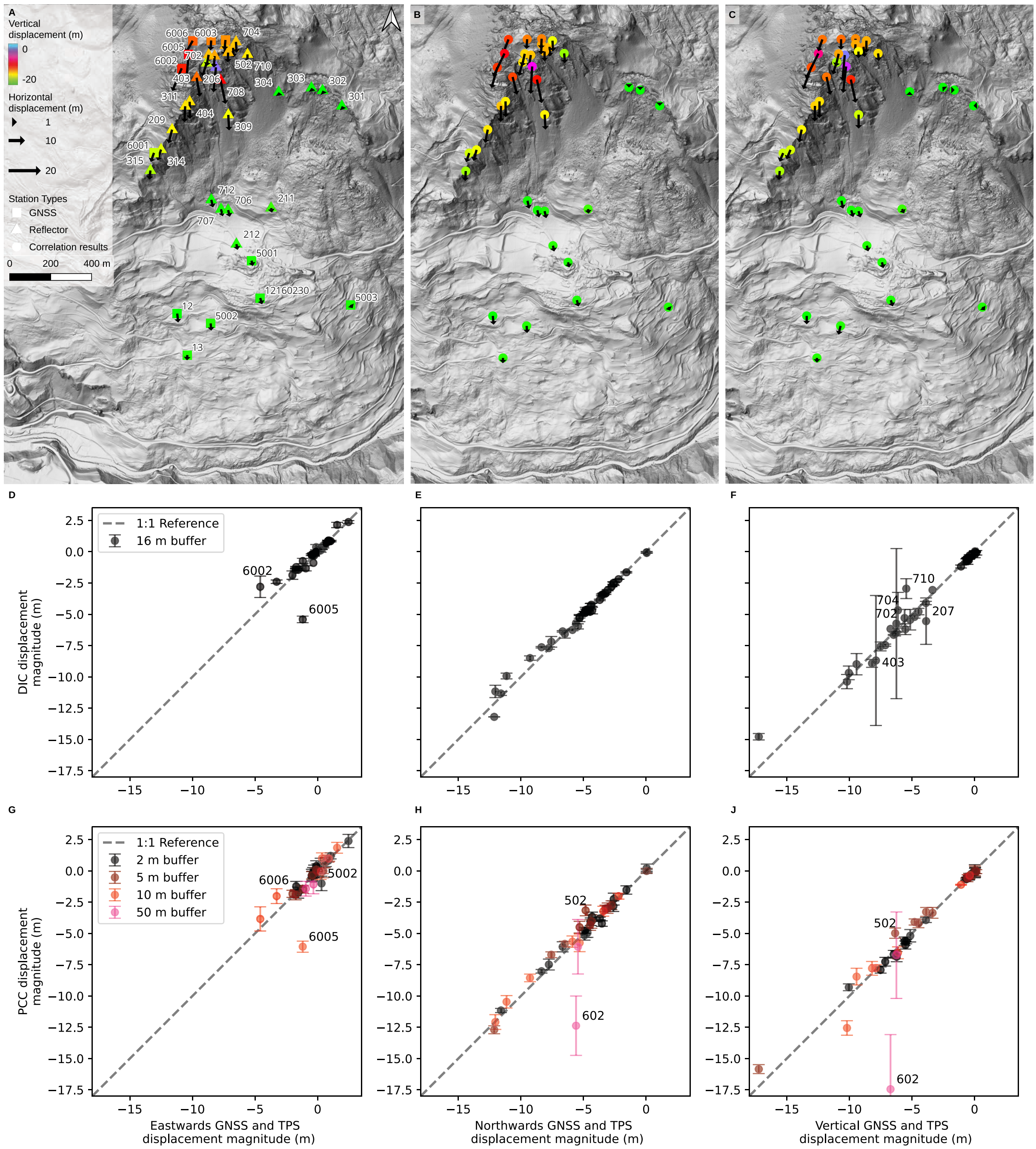

Figure 4. Comparison between methods at ground control points. **A:** GNSS and total station reflectors; **B:** DIC; **C:** PCC. Colours represent the vertical displacement, arrows represent the horizontal displacement, magnified ten times. DIC compared to ground stations in EW **(D)**, NS **(E)** and UD **(F)** with buffers of 2 m around ground stations; PCC compared to ground stations in EW **(G)**, NS **(H)** and UD **(I)** categorised by buffer distance to the ground stations, as PCC exhibits a variable spatial sampling. The background map in **A**, **B**, and **C** is taken from the Federal Office of Topography Swisstopo (2024).

https://doi.org/10.5194/egusphere-2026-5055
Preprint. Discussion started: 25 September 2026

volume of the critical compartments, thereby better evaluating the hazard they might pose. However, several limitations of DIC were also identified. Fast-moving compartments in the centre of the landslide body showed significant changes in their surface, and coherence was not maintained between the two flights, resulting in decorrelation. This intrinsic limitation is shared with PCC and other correlation methods.

The results obtained by applying our DIC approach show that we can produce 3D displacement fields in complex landslide scenarios comparable to those obtained with state-of-the-art PCC methods. Moreover, the measurements were validated by comparing them to in-situ monitoring data. In general, three major differences were identified between PCC and DIC.

First, PCC seems more sensitive to vegetation than DIC, providing fewer measurement points in these areas. In forested areas, the noise level increases significantly, likely because of the poor capacity of photogrammetric datasets to resolve these regions. Thus, PCC might be better suited for the analyses of point clouds generated with Light Detection and Ranging (LiDAR) sensors instead of photogrammetric datasets. In LiDAR results, the vegetation signal can be filtered before running point cloud correlation. Instead, DIC seems to handle vegetated areas better thanks to relatively larger correlation windows.

Secondly, the sizes of the point datasets obtained from both methods differ significantly. While both methods produce similar results at ground control points, the number of samples in PCC is much larger than in DIC (over 1 million points against less than 15'000 points, respectively). The larger dataset produced by PCC adds complexity and time to analysing, visualising, or filtering the data. Conversely, the data handling in DIC is an advantage for machines with limited computational capacity and thus more suitable for rapid assessments of surface displacements. For comparison, we ran the PCC and DIC algorithms on the same machine (Brentford ASUS PRIME Z890-P WIFI, with 24 processors Intel Core Ultra 9 285K and 256 GiB memory). PCC with a voxel size of $1\,\mathrm{m}$ took 30 minutes to run and 11.9 minutes to filter the results, while DIC processing considering the input at $1\,\mathrm{m}$ resolution and window size 64×64 pixels took 0.5 minutes and 0.01 minutes to filter the results, thus about 1% of the total time needed by the PCC. We note that in a case where the order of magnitude of maximum displacements is unknown, it might be necessary to run the DIC algorithm multiple times, changing the window size and ensuring that the maximum displacements are correctly retrieved. Also, a higher point density can be beneficial in some applications, but our method is better suited for rapid 3D displacement measurements at large scale.

Third, PCC tends to overestimate the displacement in stable areas. There, manual feature tracking performed on the DEMs confirms that the surroundings of the landslide are not moving and agrees better with the results of DIC. However, DIC is affected by a systematic bias too. Due to discrete displacement values limited to 1/10th of the pixel size, several locations are rounded to zero if moving less than $0.05\,\mathrm{m}$ is recorded in eastwards and northwards directions. This can lead to an underestimation of the displacement by DIC in slow-moving areas. We found that the vertical displacements obtained from DIC have a higher uncertainty than the horizontal ones. This can be in part attributed to the approach used to shift the secondary DEM before calculating the difference in height.

https://doi.org/10.5194/egusphere-2026-5055
Preprint. Discussion started: 25 September 2026

6 Conclusions

In this study, we presented a Digital Image Correlation (DIC) workflow for retrieving three-dimensional surface displacement fields from multi-temporal digital elevation models (DEMs). Our method explicitly corrects for the Eulerian bias in the vertical component through a shift-back procedure, avoiding artifacts generated by large horizontal motions. We validated our approach at the Brienz/Brinzauls landslide, Switzerland, using ground monitoring data. The results demonstrate that our DIC workflow can accurately measure slope displacements ranging from centimeters to tens of meters over the same slope. The method's ability to identify gradients across several orders of magnitude is crucial for describing spatial patterns of displacement and landslide compartments. We compared our DIC approach with a state-of-the-art Point Cloud Correlation (PCC) method, showing that both methods produce comparable results in complex landslide scenarios. However, we identified three major differences between PCC and DIC. PCC seems more sensitive to vegetated areas than DIC, providing fewer measurement points in these regions, while DIC handles vegetated areas better with large enough correlation windows. PCC produces a much larger dataset, adding complexity and time to data analysis, visualization, or filtering. Finally, PCC tends to overestimate displacement in stable areas, while DIC can underestimate it due to discrete displacement values limited to 1/10th of the pixel size. Our study highlights the potential of DIC for measuring surface displacements associated with geological processes in 3D. The proposed workflow is computationally efficient, making it a valuable tool for landslide monitoring and hazard assessment. Future work should explore the capacities of the DIC method to extract useful information before and during a deformation crisis, including multiple digital terrain model acquisitions.

Code and data availability. The drone images used for this study can be downloaded from https://www.doi.org/10.16904/envidat.797. The MOBI-DIC software can be requested freely for non-commercial use.

Author contributions. AM conceived the study and designed the original DIC algorithm, NO performed the F2S3 processing and the DIC sensitivity analysis. FD developed the MOBI-DIC software, prepared in-situ data and calculated the DIC results. NO and FD wrote the first draft. AM supervised the study, and contributed to writing, review and editing the final manuscript. All authors reviewed and approved the final manuscript.

Competing interests. AM is a topical editor of the journal Earth Observation (EO).

Disclaimer. Use of AI: The Overleaf AI Rewrite feature was used to rephrase selected sentences for clarity and academic tone. Grammarly was also used for a language check. Generative AI (locally hosted Qwen3 Vision 4B Instruct) was used to assist in drafting and editing the language of this paper. All content has been checked.

https://doi.org/10.5194/egusphere-2026-5055
Preprint. Discussion started: 25 September 2026

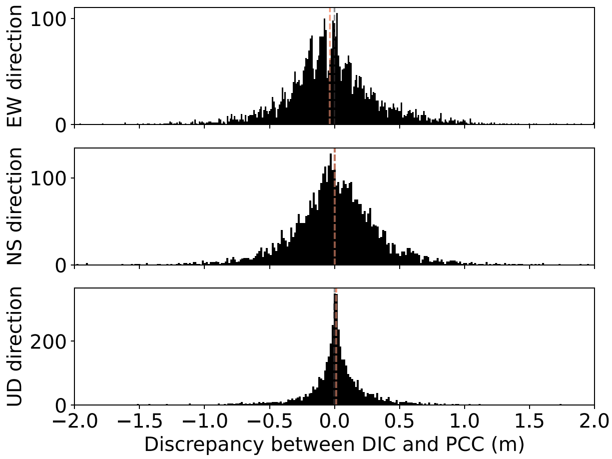

Figure A1. Histograms of the residuals between DIC and PCC, also shown in Figure 3C, D, E, and F. The red dashed line marks the median of the direction's residuals, while the grey dashed line marks the 0 line.

Acknowledgements. We thank the Büro für Technische Geologie AG, BTG, for sharing the GNSS and total station data. We thank Andreas Stoffel and Yves Bühler for sharing the drone topographic models.

Appendix A: DIC Parameter sensitivity analysis

We tested the sensitivity of the DIC method to its main parameters (the size of the correlation window and the resolution of the digital terrain models. To evaluate the correctness of a set of parameters, we consider the PCC method as reference, and measure the goodness of fit of the DIC method, pixelwise. We note that for a single set of parameters, there is a range of misfit, as shown in the histograms of Figure 1, for a window size of 64 pixels and a resolution of $1\,m$. In this example, the median of the residuals is near 0 in the three spatial directions, and most correlation windows have near-zero residuals. Spikes can be observed every $0.1\,m$ in both horizontal directions, corresponding to the ground sampling distance (GSD, $1\,m$) divided by the oversampling factor (10). However, larger spikes are visible at every meter in the horizontal directions with the PCC method (Figure A2), and correspond to the voxel size. The effect seems to be absent in the vertical direction.

The sensitivity analysis indicates that the best overall parameter set is obtained with a GSD of $1\,m$ and a window size of 64 pixels. Increasing the resolution to the maximum ($0.1\,m$) does not improve the results, even with a larger window size, because the noise level in the DEMs becomes too large. Conversely, decreasing the resolution (e.g., $10\,m$) does not improve the results, even when the window size is decreased to only a few pixels. In this case, the area with the maximum displacement magnitudes at the top of the Insel compartment (see Figure 3) exhibits underestimated displacement magnitudes. We find that the best parameter set is obtained by decreasing the resolution of the input DEMs reasonably (e.g., $1\,m$) and adapting the size of the correlation window accordingly (e.g., 32 or 64 pixels). We note that a good practice might be to test several window

https://doi.org/10.5194/egusphere-2026-5055
Preprint. Discussion started: 25 September 2026

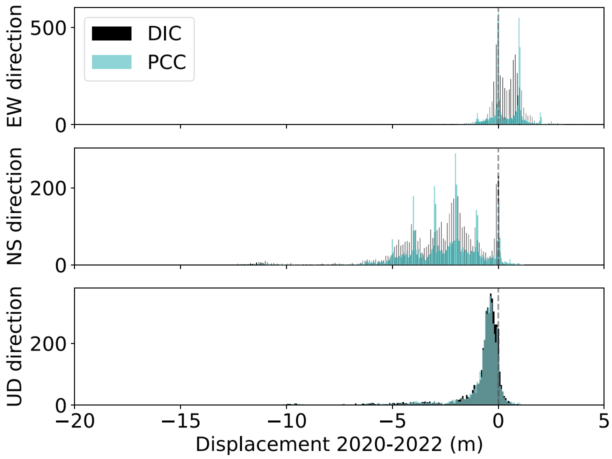

Figure A2. Histograms of displacement in the three spatial directions for the two methods DIC and PCC. The black dashed line highlights the 0 displacement mark. PCC exhibits spikes at every $1\,m$ in both horizontal directions, corresponding to the chosen voxel size. DIC shows spikes at every $0.25\,m$ in the horizontal directions, corresponding to 1/4 of a pixel, due to rounding effects.

sizes and DEM resolutions, focusing on decreasing the noise level in areas with little to no displacement, while retaining the areas with the maximum displacement magnitudes.

Appendix B: Additional visualisation of displacement data

In the following, the ground-based stations that are used in the study are shown on a map (Figure B1), with their identification numbers (the same numbers used in the text to describe their displacement trends). Figure B2 exhibits the spatial variations in dip angles and azimuth angles. Landslide compartments can be drawn based on these maps, together with the displacement magnitude map (Figure 3). The displacement magnitude for selected regions is displayed in Figure B2B with arrows showing the horizontal displacement direction and 3D displacement magnitude exaggerated 100 times.

Appendix C: Synthetic test for DIC shift-back

To validate the shift-back procedure independently of field data, we generated two Gaussian-shaped DEMs with a known applied 3D displacement ($\Delta x = 1.5\,\mathrm{m}$, $\Delta y = 0.5\,\mathrm{m}$, $\Delta z = -1.0\,\mathrm{m}$) and a superimposed synthetic texture to enable DIC matching (Figure C1 panels A and D). The texture was generated as spatially correlated Gaussian noise (white noise smoothed with a Gaussian kernel of 5 pixel correlation length, scaled to $0.5\,\mathrm{m}$ roughness amplitude) and rigidly translated together with the terrain, so that the texture pattern itself carries no spurious elevation-difference signal. A standard fixed-grid elevation difference (Eulerian DoD) produces a dipole artefact centred on the hill crest, as the horizontal translation of sloped terrain is misread as vertical change (Figure C1 panels B and E). After shift-back correction using the DIC-derived horizontal displacement, this

https://doi.org/10.5194/egusphere-2026-5055
Preprint. Discussion started: 25 September 2026

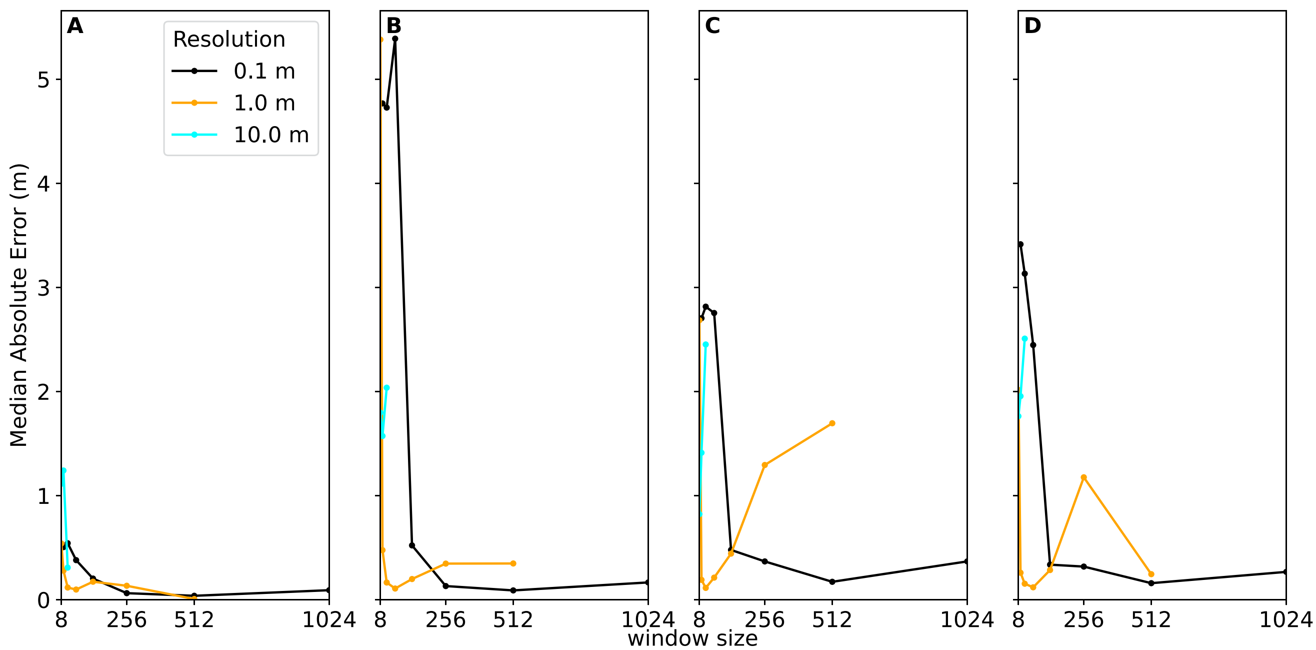

Figure A3. Influence of the DEM resolution and correlation window size on the Median AE evaluated at all ground control points in **A:** E-W, **B:** N-S, **C:** vertical directions, and **D:** 3D magnitude.

artefact is removed and the true, spatially uniform vertical displacement is recovered (Figure C1 panels C and F), confirming that the procedure correctly isolates true vertical change from displacement-induced geometric artefacts.

In addition to the shift-back procedure described above, we implemented a pixel-wise ("point-wise") Lagrangian reconstruction: the sparse per-window DIC displacement field is first interpolated to the native DEM resolution, and the vertical displacement at every DEM pixel is then computed as $dz(x,y) = \mathrm{DEM}_2(x + dx(x,y),\, y + dy(x,y)) - \mathrm{DEM}_1(x,y)$, with the elevation at the displaced position obtained by interpolation, rather than being reconstructed patch-by-patch as in the shift-back procedure. We applied this point-wise reconstruction to the same synthetic, spatially uniform displacement test described above, using nearest-neighbour, bilinear, and bicubic interpolation of the DEM at the displaced sampling position.

Figure C2A shows the resulting Eulerian DoD profile along the A-A′ cross-section, reproducing the dipole artefact shown in Figure 2C. Figure C2B compares, at a much finer vertical scale, the shift-back reconstruction against the point-wise reconstruction (bilinear interpolation shown; nearest-neighbour and bicubic interpolation produced near-identical results). Both the shift-back and the point-wise reconstruction converge closely to the imposed vertical displacement of $-1\,\mathrm{m}$, in clear contrast to the Eulerian DoD in panel A. The point-wise reconstruction retains a small residual scatter around the imposed value (standard deviation $\approx 0.06\,\mathrm{m}$, i.e. approximately $6\,\%$ of the imposed $1\,\mathrm{m}$ displacement, essentially the same for all three interpolation orders tested), whereas the shift-back reconstruction reproduces the imposed displacement exactly (standard deviation $<0.001\,\mathrm{m}$) in this idealised, noise-free synthetic test. This residual arises because the point-wise formulation samples the fine-

https://doi.org/10.5194/egusphere-2026-5055
Preprint. Discussion started: 25 September 2026

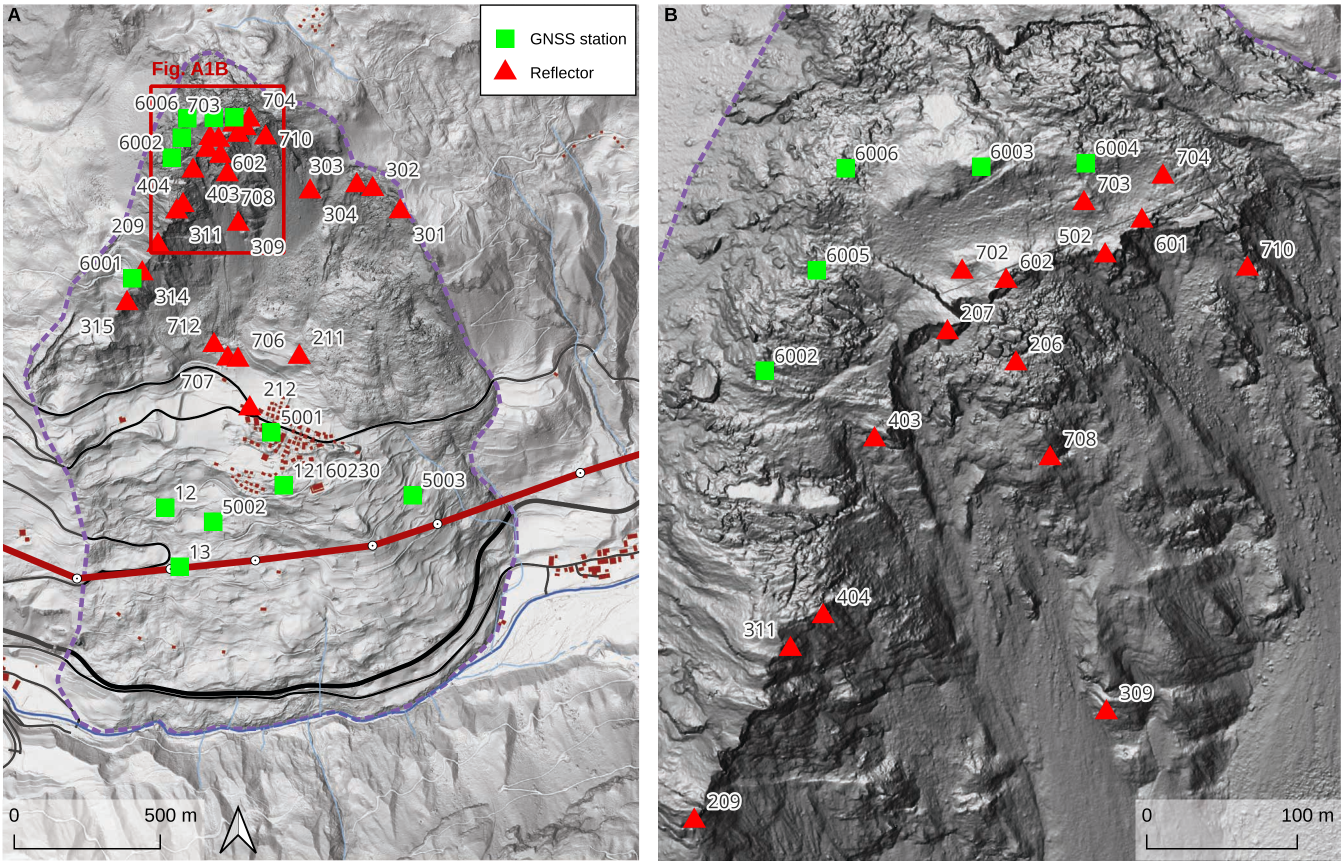

Figure B1. Station names used in this study. **A:** All stations, including GNSS (green squares) and reflectors (red triangles). **B:** Zoom in the Plateau / Pro Fop / Insel region to enlarge the area with a higher density of stations. The extent of the landslide is shown with a dashed purple line; the main roads, powerline, rivers, and buildings are shown too. The legend for these background layers is in Figure 1.

scale surface roughness superimposed on the DEMs (added to enable DIC matching, see above) individually at every pixel via local, low-order interpolation, whereas the shift-back procedure moves each entire correlation-window patch rigidly as a block, which better preserves this fine-scale surface structure.

https://doi.org/10.5194/egusphere-2026-5055
Preprint. Discussion started: 25 September 2026

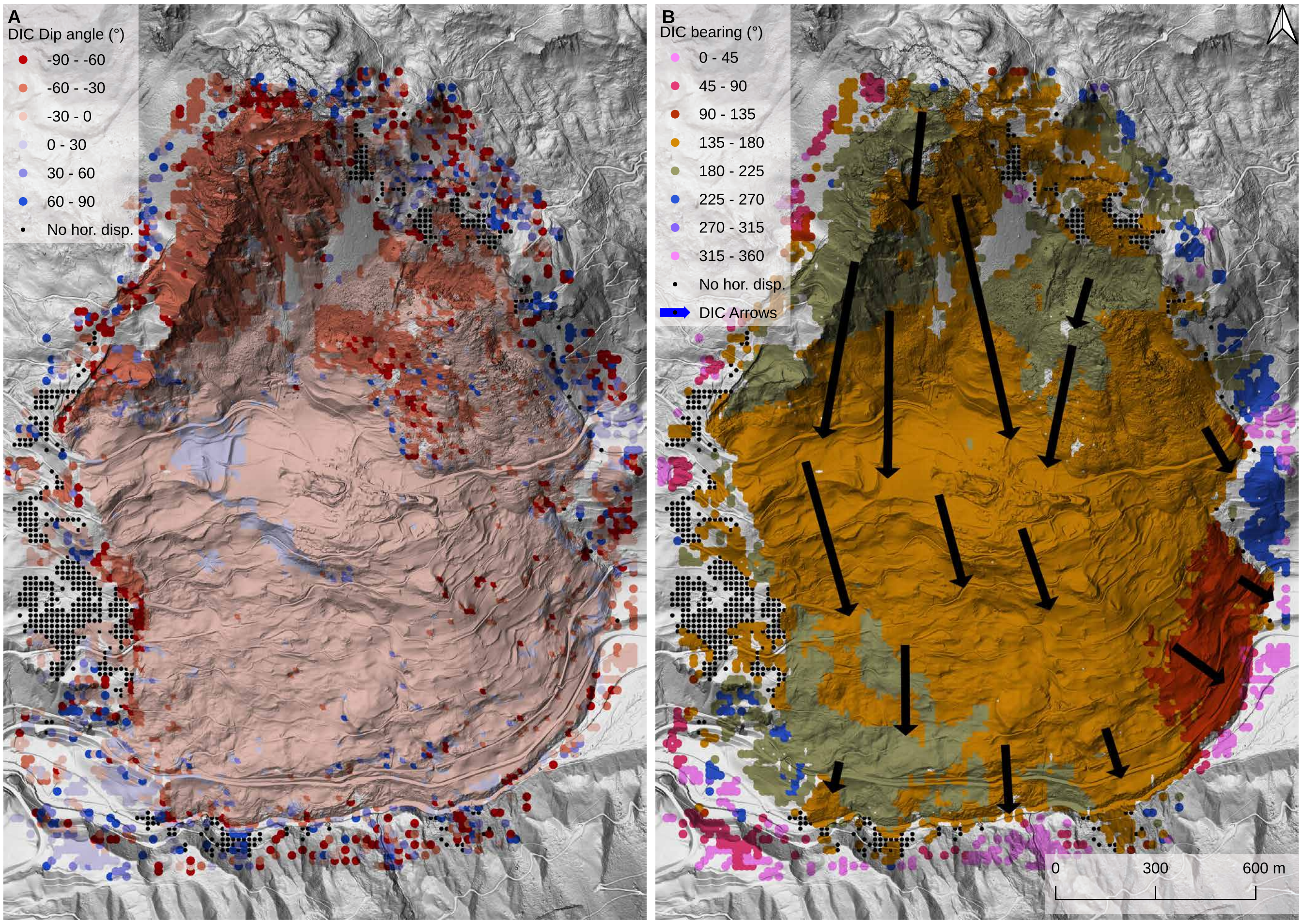

Figure B2. A: Dip and **B:** azimuth angles of displacement obtained from DIC. The extent of the landslide, some internal compartments and dynamics can be identified from the displacement patterns. Selected locations are displayed with their displacement magnitude exaggerated 100 times.

https://doi.org/10.5194/egusphere-2026-5055
Preprint. Discussion started: 25 September 2026

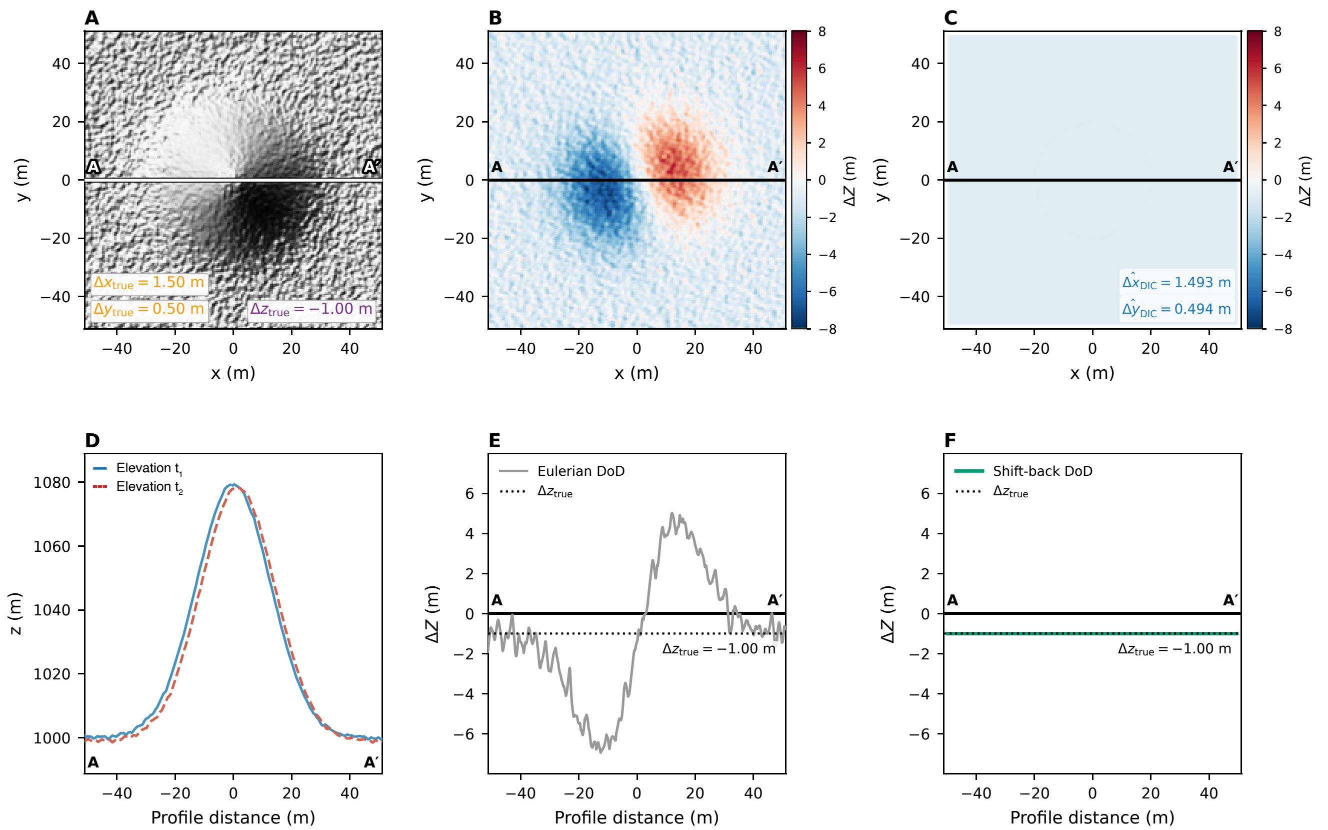

Figure C1. Synthetic validation of the shift-back procedure. **A:** Hillshade of the primary DEM with the A-A′ cross-section used in (D)-(F). **B:** Eulerian DoD map, showing the dipole artefact from horizontal displacement on sloped terrain. **C:** Lagrangian DoD map after shift-back correction, recovering the true, spatially uniform vertical displacement. **D:** Elevation profiles of DEM_1 and DEM_2 along A-A′. **E:** Eulerian DoD profile along A-A′. **F:** Lagrangian DoD profile along A-A′ after correction.

https://doi.org/10.5194/egusphere-2026-5055
Preprint. Discussion started: 25 September 2026

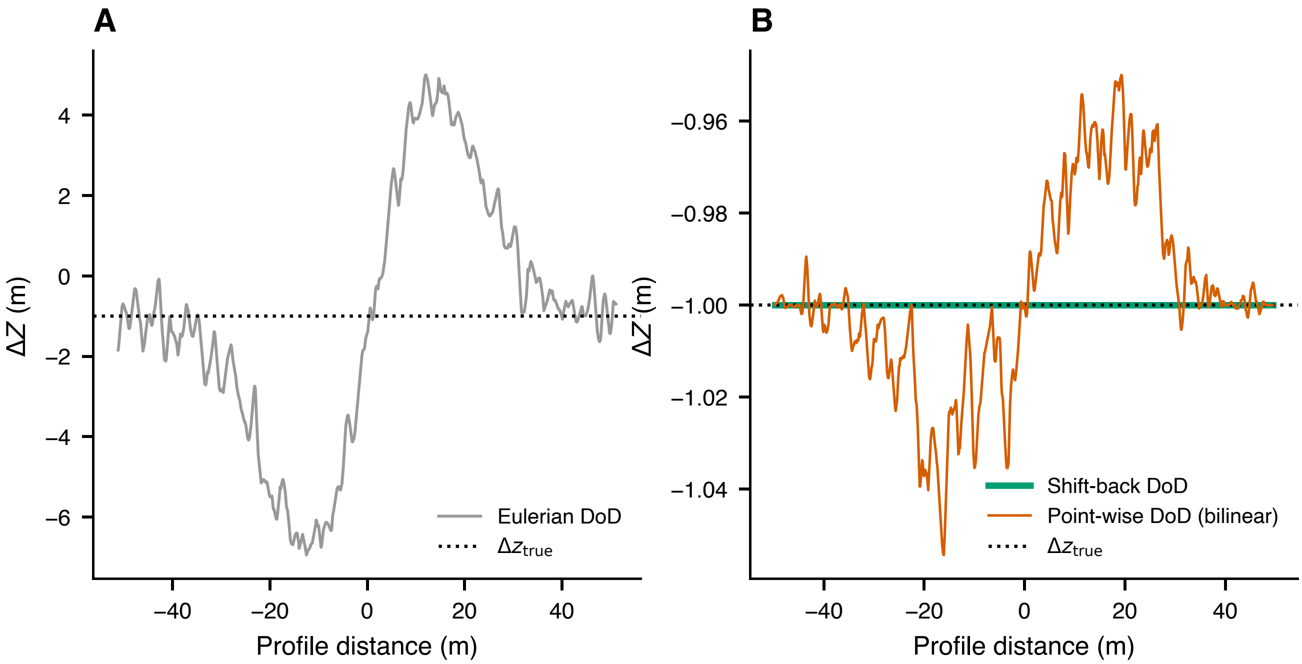

Figure C2. Comparison of vertical displacement profiles along the A-A′ cross-section for the synthetic uniform-displacement test. **A:** Eulerian DoD (grey), reproducing the dipole artefact of Figure 2C. **B:** Shift-back reconstruction (this study, green) and point-wise reconstruction (bilinear interpolation, orange), shown at a finer vertical scale to resolve their small differences. The dotted line in both panels marks the imposed $\Delta z_{\text{true}} = -1.0\,\text{m}$ displacement.

https://doi.org/10.5194/egusphere-2026-5055
Preprint. Discussion started: 25 September 2026

References

Agliardi, F., Scuderi, M. M., Fusi, N., and Collettini, C.: Slow-to-fast transition of giant creeping rockslides modulated by undrained loading in basal shear zones, Nature Communications, 11, 1–11, https://doi.org/10.1038/s41467-020-15093-3, 2020.

Anders, K., Lindenbergh, R. C., Vos, S. E., Mara, H., de Vries, S., and Höfle, B.: High-Frequency 3D Geomorphic Observation Using Hourly Terrestrial Laser Scanning Data of a Sandy Beach, ISPRS Annals of the Photogrammetry, Remote Sensing and Spatial Information Sciences, IV-2/W5, 317–324, https://doi.org/10.5194/isprs-annals-IV-2-W5-317-2019, 2019.

Aryal, A., Brooks, B. A., Reid, M. E., Bawden, G. W., and Pawlak, G. R.: Displacement fields from point cloud data: Application of particle imaging velocimetry to landslide geodesy, Journal of Geophysical Research: Earth Surface, 117, https://doi.org/10.1029/2011JF002161, 2012.

Bickel, V. T. and Manconi, A.: Decadal Surface Changes and Displacements in Switzerland, Journal of Geovisualization and Spatial Analysis, 6, 24–, https://doi.org/10.1007/S41651-022-00119-9, 2022.

Bickel, V. T., Manconi, A., and Amann, F.: Quantitative Assessment of Digital Image Correlation Methods to Detect and Monitor Surface Displacements of Large Slope Instabilities, Remote Sensing, 10, 865, https://doi.org/10.3390/rs10060865, 2018.

Borgeat, X., Glueer, F., Häusler, M., Hobiger, M., and Fäh, D.: On the variability of the site-response parameters of the active rock slope in Brienz/Brinzauls (Switzerland), Geophysical Journal International, 240, https://doi.org/10.1093/GJI/GGAE412, 2025.

Casson, B., Delacourt, C., Baratoux, D., and Allemand, P.: Seventeen years of the "La Clapière" landslide evolution analysed from ortho-rectified aerial photographs, Engineering Geology, 68, 123–139, https://doi.org/10.1016/S0013-7952(02)00201-6, 2003.

Casu, F., Manconi, A., Pepe, A., and Lanari, R.: Deformation time-series generation in areas characterized by large displacement dynamics: The SAR amplitude pixel-offset SBAS technique, IEEE Transactions on Geoscience and Remote Sensing, 49, 2752–2763, https://doi.org/10.1109/TGRS.2010.2104325, 2011.

Chanut, M.-A., Peru, Y., Faillettaz, J., Dubois, L., Carotte, A., and Azemard, P.: Automatic tracking rockfall precursory movements in 3D point clouds using the new L-ICP method, Geomorphology, 492, 110 056, https://doi.org/10.1016/j.geomorph.2025.110056, 2026.

Chu, T. C., Ranson, W. F., and Sutton, M. A.: Applications of digital-image-correlation techniques to experimental mechanics, Experimental Mechanics, 25, 232–244, https://doi.org/10.1007/BF02325092, 1985.

Debella-Gilo, M. and Kääb, A.: Sub-pixel precision image matching for measuring surface displacements on mass movements using normalized cross-correlation, Remote Sensing of Environment, 115, 130–142, https://doi.org/10.1016/J.RSE.2010.08.012, 2011.

Delacourt, C., Allemand, P., Casson, B., and Vadon, H.: Velocity field of the "La Clapière" landslide measured by the correlation of aerial and QuickBird satellite images, Geophysical Research Letters, 31, https://doi.org/10.1029/2004GL020193, 2004.

Delorme, A., Grandin, R., Klinger, Y., Pierrot-Deseilligny, M., Feuillet, N., Jacques, E., Rupnik, E., and Morishita, Y.: Complex Deformation at Shallow Depth During the 30 October 2016 Mw6.5 Norcia Earthquake: Interference Between Tectonic and Gravity Processes?, Tectonics, 39, e2019TC005 596, https://doi.org/10.1029/2019TC005596, 2020.

Dematteis, N. and Giordan, D.: Comparison of Digital Image Correlation Methods and the Impact of Noise in Geoscience Applications, Remote Sensing, 13, 327, https://doi.org/10.3390/rs13020327, 2021.

Eringen, A. C.: Mechanics of Continua, John Wiley & Sons, New York, 1967.

Federal Office of Topography Swisstopo: swissALTI3D: The high precision digital elevation model of Switzerland, 2024.

Fey, C., Rutzinger, M., Wichmann, V., Prager, C., Bremer, M., and Zangerl, C.: Deriving 3D displacement vectors from multi-temporal airborne laser scanning data for landslide activity analyses, GIScience & Remote Sensing, 52, 437–461, https://doi.org/10.1080/15481603.2015.1045278, 2015.

Figi, D., Thöny, R., Breitenmoser, T., Brunold, F., and Schwestermann, T.: Rutschung Brienz/Brinzauls (GR): Geologisch-kinematisches und hydrogeologisches Modell, Swiss Bulletin für angewandte Geologie, 27, 2022.

Froude, M. J. and Petley, D. N.: Global fatal landslide occurrence from 2004 to 2016, Natural Hazards and Earth System Sciences, 18, 2161–2181, https://doi.org/10.5194/NHESS-18-2161-2018, 2018.

Fu, S., de Jong, S. M., Nijland, W., Gravey, M., Kraaijenbrink, P., and de Haas, T.: Retrieving 4D landslide displacement using Pléiades satellite stereo pairs on the La Valette landslide, International Journal of Applied Earth Observation and Geoinformation, 140, 104 613, https://doi.org/10.1016/j.jag.2025.104613, 2025.

Gojcic, Z., Zhou, C., and Wieser, A.: F2S3: Robustified determination of 3D displacement vector fields using deep learning, Journal of Applied Geodesy, 14, 177–189, https://doi.org/10.1515/jag-2019-0044, 2020.

Gojcic, Z., Schmid, L., and Wieser, A.: Dense 3D displacement vector fields for point cloud-based landslide monitoring, Landslides 2021 18:12, 18, 3821–3832, https://doi.org/10.1007/S10346-021-01761-Y, 2021.

Guizar-Sicairos, M., Thurman, S. T., and Fienup, J. R.: Efficient subpixel image registration algorithms, Optics Letters, 33, 156, https://doi.org/10.1364/OL.33.000156, 2008.

Hanagan, C., DeLong, S. B., and Reitman, N. G.: Effect of Land Cover Type on 3D Deformation Recovery From Synthetically Deformed High Resolution Satellite Optical Imagery, Earth and Space Science, 13, https://doi.org/10.1029/2025EA004477, 2026.

Heid, T. and Kääb, A.: Evaluation of existing image matching methods for deriving glacier surface displacements globally from optical satellite imagery, Remote Sensing of Environment, 118, 339–355, https://doi.org/10.1016/J.RSE.2011.11.024, 2012.

Heim, A.: Bergsturz und Menschenleben, Der Schweizer Geograph, 1932.

Hermle, D., Keuschnig, M., Krautblatter, M., and Bickel, V. T.: Systematic Quantification and Assessment of Digital Image Correlation Performance for Landslide Monitoring, Geosciences 2023, Vol. 13, Page 371, 13, 371, https://doi.org/10.3390/GEOSCIENCES13120371, 2023.

Häusler, M., Gischig, V., Thöny, R., Glueer, F., and Donat, F.: Monitoring the changing seismic site response of a fast-moving rockslide (Brienz/Brinzauls, Switzerland), Geophysical Journal International, 229, 299–310, https://doi.org/10.1093/GJI/GGAB473, 2022.

James, M. R., Robson, S., and Smith, M. W.: 3-D uncertainty-based topographic change detection with structure-from-motion photogrammetry: precision maps for ground control and directly georeferenced surveys, Earth Surface Processes and Landforms, 42, 1769–1788, 2017.

Kenner, R., Gischig, V., Gojcic, Z., Quéau, Y., Kienholz, C., Figi, D., Thöny, R., and Bonanomi, Y.: The potential of point clouds for the analysis of rock kinematics in large slope instabilities: examples from the Swiss Alps: Brinzauls, Pizzo Cengalo and Spitze Stei, Landslides 2022 19:6, 19, 1357–1377, https://doi.org/10.1007/S10346-022-01852-4, 2022.

Kuglin, C. and Hines, D.: The phase correlation image alignment method, in: Proceedings of IEEE International Conference on Cybernetics and Society, pp. 163–165, 1975.

Kääb, A., Huggel, C., Fischer, L., Guex, S., Paul, F., Roer, I., Salzmann, N., Schlaefli, S., Schmutz, K., Schneider, D., Strozzi, T., and Weidmann, Y.: Remote sensing of glacier- and permafrost-related hazards in high mountains: an overview, Natural Hazards and Earth System Sciences, 5, 527–554, https://doi.org/10.5194/NHESS-5-527-2005, 2005.

Kääb, A., Altena, B., and Mascaro, J.: Coseismic displacements of the 14 November 2016 M_w 7.8 Kaikoura, New Zealand, earthquake using the Planet optical cubesat constellation, Natural Hazards and Earth System Sciences, 17, 627–639, https://doi.org/10.5194/nhess-17-627-2017, 2017.

Lague, D., Brodu, N., and Leroux, J.: Accurate 3D comparison of complex topography with terrestrial laser scanner: Application to the Rangitikei canyon (N-Z), ISPRS Journal of Photogrammetry and Remote Sensing, 82, 10–26, https://doi.org/10.1016/J.ISPRSJPRS.2013.04.009, 2013.

Leprince, S., Barbot, S., Ayoub, F., and Avouac, J.-P.: Automatic and Precise Orthorectification, Coregistration, and Subpixel Correlation of Satellite Images, Application to Ground Deformation Measurements, IEEE Transactions on Geoscience and Remote Sensing, 45, 1529–1558, https://doi.org/10.1109/TGRS.2006.888937, 2007.

Lewis, J. P.: Fast Normalized Cross-Correlation, Industrial Light and Magic, 10, 2001.

Loew, S., Gschwind, S., Gischig, V., Keller-Signer, A., and Valenti, G.: Monitoring and early warning of the 2012 Preonzo catastrophic rockslope failure, Landslides, 14, 141–154, https://doi.org/10.1007/s10346-016-0701-y, 2017.

Loew, S., Schneider, S., Josuran, M., Figi, D., Thoeny, R., Huwiler, A., Largiadèr, A., and Naenni, C.: Early warning and dynamics of compound rockslides: lessons learnt from the Brienz/Brinzauls 2023 rockslope failure, Landslides, 22, 283–298, https://doi.org/10.1007/S10346-024-02380-Z/FIGURES/12, 2025.

Lucieer, A., Jong, S. M., and Turner, D.: Mapping landslide displacements using Structure from Motion (SfM) and image correlation of multi-temporal UAV photography, Progress in Physical Geography, 38, 97–116, https://doi.org/10.1177/0309133313515293, 2014.

Mackenzie, D. and Elliott, A.: Untangling tectonic slip from the potentially misleading effects of landform geometry, Geosphere, p. GES01386.1, https://doi.org/10.1130/GES01386.1, 2017.

Manconi, A., Casu, F., Ardizzone, F., Bonano, M., Cardinali, M., Luca, C. D., Gueguen, E., Marchesini, I., Parise, M., Vennari, C., Lanari, R., and Guzzetti, F.: Brief Communication: Rapid mapping of landslide events: the 3 December 2013 Montescaglioso landslide, Italy, Natural Hazards and Earth System Sciences, 14, 1835–1841, https://doi.org/10.5194/nhess-14-1835-2014, 2014.

Manconi, A., Jones, N., Loew, S., Strozzi, T., Caduff, R., and Wegmueller, U.: Monitoring surface deformation with spaceborne radar interferometry in landslide complexes: insights from the Brienz/Brinzauls slope instability, Swiss Alps, Landslides, 21, 2519–2533, https://doi.org/10.1007/S10346-024-02291-Z/FIGURES/8, 2024.

Nissen, E., Maruyama, T., Arrowsmith, J. R., Elliott, J. R., Krishnan, A. K., Oskin, M. E., and Saripalli, S.: Coseismic fault zone deformation revealed with differential lidar: Examples from Japanese Mw $\sim$7 intraplate earthquakes, Earth and Planetary Science Letters, 405, 244–256, https://doi.org/10.1016/J.EPSL.2014.08.031, 2014.

Pastor, M., Haddad, B., Sorbino, G., Cuomo, S., and Drempetic, V.: A depth-integrated, coupled SPH model for flow-like landslides and related phenomena, International Journal for Numerical and Analytical Methods in Geomechanics, 33, 143–172, https://doi.org/10.1002/nag.705, 2008.

Peters, W. H. and Ranson, W. F.: Digital image techniques in experimental stress analysis, Optical Engineering, 21, 427–431, 1982.

Petley, D. N., Mantovani, F., Bulmer, M. H., and Zannoni, A.: The use of surface monitoring data for the interpretation of landslide movement patterns, Geomorphology, 66, 133–147, https://doi.org/10.1016/J.GEOMORPH.2004.09.011, 2005.

Scherler, D., Leprince, S., and Strecker, M.: Glacier-surface velocities in alpine terrain from optical satellite imagery—Accuracy improvement and quality assessment, Remote Sensing of Environment, 112, 3806–3819, https://doi.org/10.1016/j.rse.2008.05.018, 2008.

https://doi.org/10.5194/egusphere-2026-5055
Preprint. Discussion started: 25 September 2026

Schneider, M., Oestreicher, N., Ehrat, T., and Loew, S.: Rockfall monitoring with a Doppler radar on an active rockslide complex in Brienz/Brinzauls (Switzerland), Natural Hazards and Earth System Sciences, 23, 3337–3354, https://doi.org/10.5194/nhess-23-3337-2023, 2023.

Stumpf, A., Malet, J. P., Allemand, P., and Ulrich, P.: Surface reconstruction and landslide displacement measurements with Pléiades satellite images, ISPRS Journal of Photogrammetry and Remote Sensing, 95, 1–12, https://doi.org/10.1016/j.isprsjprs.2014.05.008, 2014.

Sutton, M., Wolters, W., Peters, W., Ranson, W., and McNeill, S.: Determination of displacements using an improved digital correlation method, Image and Vision Computing, 1, 133–139, https://doi.org/10.1016/0262-8856(83)90064-1, 1983.

Sutton, M. A., Orteu, J.-J., and Schreier, H.: Image Correlation for Shape, Motion and Deformation Measurements: Basic Concepts,Theory and Applications, Springer US, Boston, MA, ISBN 978-0-387-78746-6 978-0-387-78747-3, https://doi.org/10.1007/978-0-387-78747-3, 2009.

Travelletti, J., Delacourt, C., Allemand, P., Malet, J. P., Schmittbuhl, J., Toussaint, R., and Bastard, M.: Correlation of multi-temporal ground-based optical images for landslide monitoring: Application, potential and limitations, ISPRS Journal of Photogrammetry and Remote Sensing, 70, 39–55, https://doi.org/10.1016/j.isprsjprs.2012.03.007, 2012.

Travelletti, J., Malet, J. P., and Delacourt, C.: Image-based correlation of Laser Scanning point cloud time series for landslide monitoring, International Journal of Applied Earth Observation and Geoinformation, 32, 1–18, https://doi.org/10.1016/j.jag.2014.03.022, 2014.

Wang, Z., Butt, J. A., Huang, S., Medić, T., and Wieser, A.: Dense 3D displacement estimation for landslide monitoring via fusion of TLS point clouds and embedded RGB images, International Journal of Applied Earth Observation and Geoinformation, 146, 105 093, https://doi.org/10.1016/J.JAG.2026.105093, 2026.

Winiwarter, L., Anders, K., and Höfle, B.: M3C2-EP: Pushing the limits of 3D topographic point cloud change detection by error propagation, ISPRS Journal of Photogrammetry and Remote Sensing, 178, 240–258, https://doi.org/10.1016/J.ISPRSJPRS.2021.06.011, 2021.

Zhou, Y., Parsons, B., Elliott, J. R., Barisin, I., and Walker, R. T.: Assessing the ability of Pleiades stereo imagery to determine height changes in earthquakes: A case study for the El Mayor-Cucapah epicentral area, Journal of Geophysical Research: Solid Earth, 120, 8793–8808, https://doi.org/10.1002/2015JB012358, 2015.